Targeted Therapy for Glioblastoma Multiforme using Biofunctionalized Iron Oxide Nanoparticles and Deep Learning-Enhanced Method

Vishnu Priya Kancharla
Sri Padmavati Mahila Visvavidyalayam
John Sushma Nannepaga
johnsushma@gmail.com

Sri Padmavati Mahila Visvavidyalayam
Mannur Ismail Shaik
Universiti Malaysia Terengganu
Mhd Ikhwanuddin Bin Abdullah
Universiti Malaysia Terengganu
Norizah Mhd Sarbon
Universiti Malaysia Terengganu

Research Article

Keywords: Glioblastoma multiforme (GBM), T. cordifolia, convolutional neural networks (CNNs), FeO nanoparticle, Deep Learning-Enhancement

Posted Date: April 2nd, 2026

DOI: https://doi.org/10.21203/rs.3.rs-9067475/v1

Additional Declarations: No competing interests reported.

Targeted Therapy for Glioblastoma Multiforme using Biofunctionalized Iron Oxide Nanoparticles and Deep Learning-Enhanced Method

Vishnu Priya Kancharla[1], John Sushma Nannepaga[1*], Mannur Ismail Shaik[2#], Mhd Ikhwanuddin Bin Abdullah[3], Norizah Mhd Sarbon[2]

[1]*Department of Biotechnology, Sri Padmavati Mahila Visvavidyalayam, Tirupati-524502, Andhra Pradesh, India.*

[2]*Faculty of Food Science and Agrotechnology, Universiti Malaysia Terengganu, 21030 Kuala Nerus, Terengganu, Malaysia.*

[3]*Institute of Tropical Aquaculture and Fisheries, Universiti Malaysia Terengganu, 21030 Kuala Nerus, Terengganu, Malaysia.*

***Corresponding author:**

Prof. John Sushma Nannepaga

Department of Biotechnology, Sri Padmavati Mahila Visvavidyalayam, Tirupati, A.P, India.

Email: johnsushma@gmail.com

#Corresponding author:

Dr. Mannur Ismail Shaik

Faculty of Food Science and Agrotechnology, Universiti Malaysia Terengganu, 21030 Kuala Nerus, Terengganu, Malaysia.

Email: mannurismail@umt.edu.my

Abstract

Glioblastoma multiforme (GBM) remains one of the most aggressive and treatment-resistant brain tumors, largely due to its infiltrative nature and the presence of the blood brain barrier, which limits effective drug delivery. In this study, we explored the potential of biofunctionalized iron oxide nanoparticles (FeONPs) synthesized using *Tinospora cordifolia* (*T. cordifolia)* leaf extract as a targeted therapeutic platform for glioblastoma treatment, supported by deep learning enhanced analytical methods. The green synthesis approach enabled the formation of stable and biocompatible FeONPs, as confirmed by UV–visible spectroscopy, FTIR, XRD, and TEM analyses. FTIR results indicated the involvement of plant-derived functional groups such as hydroxyl, amine, carbonyl, and C–O groups in nanoparticle stabilization, while XRD confirmed their crystalline magnetite/maghemite phase. TEM analysis revealed predominantly rod-shaped nanoparticles with nanoscale dimensions. The synthesized FeONPs exhibited notable antioxidant activity and demonstrated dose-dependent cytotoxic effects on glioblastoma and neuronal cell lines, highlighting their therapeutic relevance. Owing to their magnetic properties, surface biofunctionalization, and favorable morphology, these FeONPs offer a promising platform for targeted delivery and potential imaging applications in GBM. Furthermore, the integration of deep learning-based methods provides a powerful tool for analyzing nanoparticle behavior, optimizing targeting efficiency, and enabling precision-driven therapeutic strategies. Overall, this study presents a multidisciplinary approach combining green nanotechnology and artificial intelligence, laying the groundwork for the development of effective and targeted therapies for glioblastoma multiforme.

Keywords: Glioblastoma multiforme (GBM), *T. cordifolia,* convolutional neural networks (CNNs), FeO nanoparticle, Deep Learning-Enhancement.

Introduction

Glioblastoma multiforme (GBM) is the most common and primary malignant brain tumor in adults [1]. Despite improvements in imaging, surgical techniques, radiotherapy, and chemotherapeutic protocols, the prognosis for GBM remains poor, with survival period of only 14 -18 months and a five-year survival rate below 5% [2]. This poor outcome arises from the tumor's infiltrative nature, intratumoral heterogeneity, resistance to therapy, and the protective role of the blood–brain barrier (BBB), which significantly restricts drug entry to the tumor site [3]. Consequently, there is an urgent need for advanced therapeutic strategies capable of selectively targeting GBM cells, overcoming drug-delivery barriers, and minimizing systemic toxicity.

In recent years, nanotechnology has emerged as a transformative approach for cancer therapy, particularly for diseases limited by inefficient drug delivery. Among various nanocarriers, iron oxide nanoparticles (FeONPs) have gained attention due to their biocompatibility, magnetic responsiveness, surface tunability, and ability to cross biological barriers through magnetic guidance or functional modifications [4]. Their inherent magnetic properties also make them promising tools for both therapeutic delivery and imaging applications. Surface coating of FeONPs with polymers such as polyvinylpyrrolidone (PVP) enhances their stability, prevents aggregation, and improves circulation time within biological systems [5]. Functionalization of these nanoparticles with biologically active herbal extracts further increases their therapeutic potential, providing combined benefits of targeted nanocarrier delivery and inherent bioactivity of plant-derived compounds.

Tinospora cordifolia (T. cordifolia), a medicinal plant widely used in traditional Indian systems of medicine, possesses well-documented antioxidant, immunomodulatory, anti-inflammatory, and anticancer properties [6]. Biofunctionalization of PVP coated FeO nanoparticles with *T. cordifolia* extract offers a promising strategy to enhance biocompatibility

and introduce natural therapeutic moieties capable of attenuating oxidative stress and inducing apoptosis in cancer cells. Such hybrid nano-formulations have been increasingly explored for synergistic anticancer effects, reduced systemic toxicity, and enhanced cellular uptake [7]. This approach aligns with the growing trend toward green nanotechnology, which seeks to integrate plant-derived phytochemicals with inorganic nanoparticles to produce environmentally benign and biologically active nanomedicines.

Beyond therapeutic interventions, advances in artificial intelligence (AI) have opened new avenues for rapid and precise cancer diagnosis. Deep learning, particularly convolutional neural networks (CNNs), has demonstrated superior accuracy in classifying medical images, detecting tumor boundaries, and distinguishing between diseased and healthy cell populations [8]. In GBM research, AI-based tools are increasingly being used to analyze histopathological and microscopic images, enabling objective quantification of cellular responses to therapeutic agents. Integrating deep learning with nanotechnology-driven therapeutics creates a powerful platform capable of both treating and monitoring disease progression with improved accuracy. Microscopic image analysis plays an essential role in the diagnosis and evaluation of cancerous tissues. Traditional image classification approaches rely heavily on handcrafted features, such as texture descriptors and morphological metrics, which can fail to capture subtle variations in complex biomedical images. In recent years, deep learning, especially Convolutional Neural Networks (CNNs), has emerged as a powerful alternative for extracting hierarchical representations directly from raw image data, leading to significant improvements in classification performance. LeCun et al. provided the foundational framework for deep learning, demonstrating that neural networks with multiple layers can learn abstract representations and outperform classical machine learning methods in image recognition tasks [9]. Building on this, developed the AlexNet architecture, which achieved breakthrough performance on the ImageNet dataset using deep convolutional neural networks, inspiring

further adoption of CNNs in domain-specific image analysis [10]. In the context of medical imaging, surveyed deep learning applications across diverse modalities, illustrating the effectiveness of CNNs in dermatology, radiology, and pathology, and highlighting their superior performance compared to traditional feature-based approaches [11]. Similarly, emphasized the transformative impact of deep learning on cellular image analysis, particularly for automated classification and segmentation tasks in microscopy [12]. Biomedical image classification has been explored for various cancer types. For example, demonstrated dermatologist-level classification of skin cancer using deep neural networks, showing deep learning's potential in clinical decision support systems [13]. Although focused on radiological images, presented 3D CNN models for brain tumor analysis, indicating that deep neural networks can effectively capture spatial patterns in volumetric medical data [14]. Specific to microscopic and histological images, U-Net architectures proposed by Ronneberger et al. have become standard for biomedical segmentation, often serving as preprocessing steps for classification workflows [15]. Fernandez et al. explored feature-fusion hybrid models for brain tumor classification, reinforcing that deep learning integration improves performance over handcrafted features [16]. Despite significant research in deep learning for histopathology and cellular imaging, there is limited work focused on treatment response classification (treated vs untreated) in glioblastoma microscopy. Most existing studies emphasize tumor detection or segmentation rather than post-treatment morphological changes. This gap highlights the need for specialized classification models capable of distinguishing subtle cellular responses to therapy, which can improve treatment monitoring and outcome prediction. Furthermore, dataset availability and standardized benchmarks remain challenges. The Cancer Imaging Archive (TCIA), providing public access to cancer imaging datasets, but datasets explicitly labeled for treatment status in glioblastoma microscopy are scarce, necessitating custom dataset collection and annotation. MATLAB's Deep Learning Toolbox and Image Processing Toolbox

play an important role in implementing CNNs for biomedical applications [17]. These toolboxes offer prebuilt layers, training functions, and visualization tools that streamline the development of deep learning models, especially in academic and research environments.

The present study aims to develop a biofunctionalized PVP coated FeO nanoparticle system using *T. cordifolia* extract, evaluate its physicochemical characteristics, and assess its antioxidant and cytotoxic potential against glioblastoma cells. Furthermore, the study incorporates a deep learning-based image classification model to analyze microscopic images of treated and untreated GBM cells, providing an intelligent tool for high-throughput monitoring of therapeutic outcomes. By combining nanomedicine and artificial intelligence, this work proposes a dual diagnostic-therapeutic strategy (theranostic approach) that addresses major limitations in GBM therapy: poor drug delivery, limited specificity, and inadequate diagnostic precision.

Materials and methods

Plant material

Fresh leaves of *Tinospora cardifolia* were collected from the local region of Tirupati, Andhra Pradesh, India. To ensure cleanliness, the leaves were washed under running tap water to eliminate any dust particles and air dried at the room temperature.

Preparation of Leaf extract

The leaf extract was prepared by macerating the leaves in the motor & pestle using the methanol as a solvent and the finely ground methanolic leaf extract was subjected to percolation by using a magnetic stirrer (48–72 h). The resulting extract was filtered twice using Whatman No.1 filter paper and stored at 4 °C for subsequent analyses.

Screening for phytochemical compounds

Phytochemical components such as alkaloids, flavonoids, phenols, tannins, saponins, terpenoids, steroids, glycosides and sugars were detected in *T. cordifolia* leaf extract using standard procedures

Test for alkaloids:

Extract was dissolved individually in dilute hydrochloric acid and filtered. Then the filtrates treated with Wagner s reagent (1.27 g of iodine and 2 g of KI along with 100 mL of distilled water). Formation of brown (reddish brown) precipitate indicates the presence of alkaloids .

Test for flavonoids:

0.05 g of the extract was treated with few drops of 10% (w/v) sodium hydroxide solution and a few drops of concentrated H_2SO_4. There was no formation of yellow color indicates the absence of favonoid.

Test for phenols:

0.05 g of the extract was treated with few drops of 5% (w/v) ferric chloride solution. Formation of bluish black (blue or green) color indicates the presence of phenol.

Test for saponins :

0.05 g of the extract was diluted with 20 mL of distilled water vigorously shaken in a graduated cylinder for 15 min. Formation of 1 cm layer of foam indicates the presence of saponins.

Test for glycosides:

0.05 g of powdered extract was diluted with 5 mL water followed by the addition of 2 mL of glacial acetic acid and a drop of ferric chloride solution. To this, 1 mL of concentrated sulphuric acid was added very slowly. The appearance of a brown ring at the interface shows the presence of glycosides.

Test for tannins:

5 g of extract was mixed into with 10 mL of distilled water. The mixture was boiled for 5 min. The production of greenish precipitate up on the addition of 2 drops of 5% FeCl3 shows the presence of Tannins.

Test for steroids:

50 mg of the extract was dissolved in 1 mL of chloroform and sulphuric acid were carefully added to form a lower layer. A reddish brown color at the interface shows the presence of steroidal ring.

Test for terpenoids:

2 ml of chloroform was added to plant extracts (0.5 g) in a test tube. Then 3 mL of concentrated sulfuric acid was added to this mixture that result in reddish brown interface confirming the presence of terpenoids

Test for sugars:

1 ml of water and 5–8 drops of Fehling's solution was added to a 0.5 g of the sample and heated over water bath. The formation of brick red precipitate indicates the presence of reducing sugars

Preparation of FeONPs

The methanolic leaf extract of *T. cordifolia* was taken for the preparation of TC-FeONPs. About 50 ml of 1 M solution of $FeCl_3$ and 50 ml of 1M $FeCl_2$ was prepared and both the solutions were mixed in an Erlenmeyer flask. To that mixture added 1g of Polyvinylpyrrolidone. Then, 25 ml of *T. cordifolia* leaf extract was added to the 100 ml of 1M Ferric chloride solution at room temperature and stirred for a few minutes. After proper mixing of the plant extract with $FeCl_3$ solution, 0.5M NaoH was added drop wise. A change in the solution's color from green to orange and then to brown indicated the formation of FeONPs. The resultant solution was centrifuged at 10,000 rpm for 10 mins, the pellet was collected, air dried at room temperature and grounded into fine powder and stored for subsequent analyses.

This synthesis method for FeONPs with *T. cordifolia* leaf extract in organic solvent is considered a pure green and eco-friendly process, as it does not involve harmful chemicals [18].

Characterization of FeONPs

The TC-FeONPs were prepared by reducing the Ferric chloride ion solution with *T. cordifolia* leaf extract and characterized using various techniques including, UV-visible spectroscopy (UV–vis), Transmission Electron Microscope (TEM), Fourier Transform Infrared Spectroscopy (FTIR) and X-Ray Diffraction (XRD)

UV-visible spectrophotometer

The methanolic extract of biofunctionalized FeONPs synthesized using *T. cordifolia* leaf was subjected to UV-visible spectroscopy (Shimadzu Model No. UV – 1800, ENG 240 V). Spectra of the suspension was collected and analyzed within the wavelength range of 300 - 450 nm.

Fourier transform infrared spectroscopy (FTIR)

The FTIR analysis was performed using a 1600 Perk-inElmerÒ spectrophotometer (PerkinElmer do Brasil Ltda, Sa˜o Paulo, SP, Brazil) in the range of 4000–400 cm^{-1}. The spectrum of the methanolic extract of biofunctionalized FeONPs synthesized using *T. cordifolia* leaf was taken, a pinch of synthesized nanoparticles was placed over the FTIR instrument, and the spectrum was recorded.

Transmission electron microscope (TEM)

The size and morphology of the FeONPs of methanolic *T. cordifolia* leaf extract was investigated using a field emission transmission electron microscope. Thin films of the sample were prepared on a carbon-coated copper grid, and the samples were allowed to dry before examination.

X-ray diffraction (XRD)

The XRD analysis for FeONPs of methanolic *T. cordifolia* leaf extract was performed using AERIS PAN analytical Instrument to identify the crystalline nature of the sample.

Determination of anti-oxidant activity

The anti-oxidant activity of FeONPs derived from methanolic *T. cordifolia* leaf extract was evaluated by using DPPH free radical scavenging assay. Different dilutions of the standard (Ascorbic acid) (10,20,40,60,80,100µg/ ml) were mixed with 1 ml of DPPH solution (0.004 % in ethanol) and incubated at 37 ◦C for 30 min. The absorbance of the mixture was measured at 517 nm using a UV–vis spectrophotometer [19]. The following formula was used to calculate the DPPH scavenging activity: % RSA= ((Absorbance of control (A0)-Absorbance of sample(A)) / (Absorbance of control) X 100) where A is the absorbance of the sample containing extract and A0 is the absorbance of the negative control (0.004 % DPPH solution).

***In vitro* Evaluation of TC-FeONPs Effects on Cell Proliferation in U-87 MG, PC-12, and HMC3 Cells Using the MTT Assay**

Maintenance of Cell line:

The U-87 MG (Human Glioblastoma astrocytoma cell line) and PC-12 (Rat Pheochromocytoma cell line) cell lines were purchased from NCCS, Pune, India. The cells were maintained in MEM with NEAA mixture supplemented with 10 % FBS along with the 1% antibiotic-antimycotic solution in the atmosphere of 5% CO_2, 18-20% O_2 at 37^0C temperature in the CO_2 incubator and sub-cultured for every 2 days. Passage numbers of U-87 MG and PC-12 cells were P28 and P21 was used for the present study.

The HMC-3 (Human Miocroglial cell line) cell lines was purchased from ATCC, USA. The cells were maintained in MEM with NEAA mixture supplemented with 10 % FBS along with the 1% antibiotic-antimycotic solution in the atmosphere of 5% CO_2, 18-20% O_2 at 37^0C temperature in the CO_2 incubator and sub-cultured for every 2 days. Passage numbers of HMC3 cells was P14 was used for the present study.

After reaching 80% of density, cells were detached by using 0.025% trypsin and 0.01% EDTA (in D-PBS) solution. Cell viability and count were performed using hemocytometer. The appropriate density of cells was seeded in T25 flasks and cultured until further usage of cells to conduct cell-based assays.

Cell viability and proliferation studies: MTT assay:

The cytotoxicity effect of TC-FeONPs was analyzed on U-87 MG, PC-12 and HMC-3 cells by performing the MTT assay. MTT is a tetrazolium salt which is converted into insoluble purple-colored formazan crystals by the action of lactate dehydrogenase enzyme released by mitochondria. Briefly, cells in 200µl of suitable media and at a density of 15,000 were plated in a 96-well plate and incubated at 37°C for overnight. After attachment of cells to the surface of cell culture plate, the spent medium was replaced with MEM having various working concentrations of TC-FeONPs (mentioned in the excel sheet). Temozolamide with 10ug/ml was used as a reference control for the study. After drug addition, cells were incubated for 24h at 37°C with 5% CO_2 atmosphere. After incubation, cells were treated with 100µL of MTT (0.5 mg/mL) was added and incubated for 3hr at 37°C. DMSO (100µL) was used to dissolve the formazan crystals, and purple color was measured at 570 nm using microplate reader (ELX-800, BioTek, USA). The viability of cells treated with MEM alone was considered as 100%. % cell viability is calculated using the below formula:

$$\% \text{ cell viability} = [\text{OD of treated cells}/\text{OD of Untreated cells}] * 100$$

The IC_{50} value was determined by using linear regression equation i.e. Y =Mx+C. Here, Y = 50, M and C values were derived from the viability graph.

Cell morphological assessment

Morphological changes in U-87 MG, PC-12 and HMC-3 cells were assessed post-treatment with given test compound with concentrations ranging from 6.25uG/ml to 200uG/ml

for 24hours at 37°C. Cells were observed and recorded by using Inverted Biological Microscope (CKX-41, Olympus) with help of camera and recorded using MICAM software at 20x magnification. Scale: 100uM.

CNN machine learning model

The methodology adopted in this project focuses on developing a convolutional neural network (CNN) to classify microscopic images of glioblastoma cells into treated and untreated categories. The overall workflow includes dataset preparation, image preprocessing, CNN model design, training, testing, and performance evaluation. Preprocessing, data augmentation, CNN architecture design, model training, and performance evaluation are all included in the suggested technique.

Study Design and Workflow

The proposed deep learning–based image classification model was implemented using MATLAB R2025**,** employing the Image Processing Toolbox and Deep Learning Toolbox. Microscopic images of glioblastoma cells were categorized into two classes: treated and untreated. The dataset was divided into training and testing subsets using an 80:20 split to ensure unbiased evaluation. All input images were resized to a uniform resolution and preprocessed to reduce noise and enhance contrast. A custom Convolutional Neural Network (CNN) architecture was designed and trained using the stochastic gradient descent with momentum (SGDM) optimizer. Model performance was evaluated using standard metrics including accuracy, precision, recall, F1-score, and a confusion matrix**.**

System Architecture

The suggested method classifies ovarian tissue pictures into normal and malignant groups using supervised deep learning. To improve quality and consistency, microscopic ovarian pictures are first obtained and pre-processed. A CNN model that automatically extracts

hierarchical features and carries out classification is then given the processed pictures. The final result shows if ovarian cancer is present or not.

Dataset Collection and Organization

Microscopic images of glioblastoma cells were collected from publicly available biomedical image repositories and curated datasets. The dataset consists of two classes:

Class 1: Treated glioblastoma cell images

Class 2: Untreated glioblastoma cell images

All images were organized into separate directories corresponding to their class labels. This folder-based structure allows automatic label assignment during data loading in MATLAB using the Image Data store utility.

Image Preprocessing

To enhance data quality and guarantee CNN model compatibility, image preparation is an essential step. The following preprocessing steps are applied to every image:

Resizing:

All images are resized to a fixed resolution to maintain uniform input dimensions for the CNN.

Normalization:

Pixel intensity values are normalized to a standard range to stabilize and accelerate model convergence.

Noise Removal:

Low-quality images and artifacts introduced during acquisition are eliminated to enhance feature clarity. Noise reduction plays a vital role in analyzing microscopic images of glioblastoma cells treated with biofunctionalized iron oxide nanoparticles. By applying average and median filtering techniques, image quality is enhanced, enabling accurate detection of morphological changes induced by targeted therapy. These preprocessed images serve as high-

quality inputs to the deep learning model, improving classification accuracy and treatment response assessment.

Average Filter

The average filter is a linear spatial smoothing filter used to reduce noise in digital images. It works by replacing each pixel value with the average of its neighbouring pixels within a defined window (such as 3×3 or 5×5). This process smooths intensity variations and reduces random noise in microscopic images.

In this project, the average filter helps reduce high-frequency noise present in glioblastoma cell images acquired during nanoparticle-based treatment experiments. However, excessive averaging may lead to blurring of cell boundaries, which can affect feature extraction.

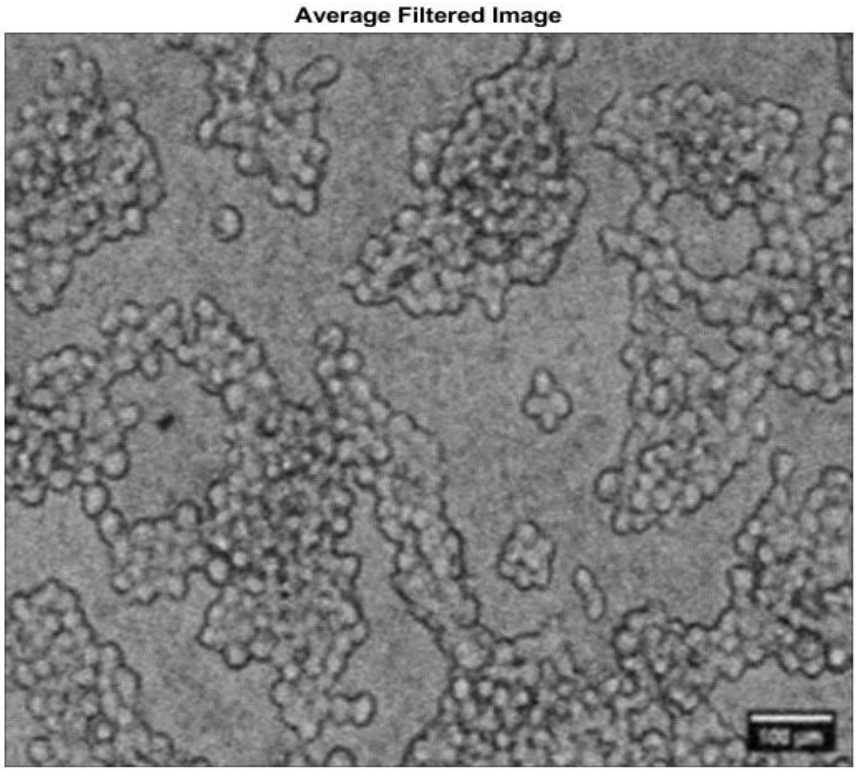

Fig 1. Application of average filtering for noise reduction in microscopic glioblastoma cell images.

Median Filter

The median filter is a non-linear filtering technique particularly effective for removing impulse noise. Instead of averaging pixel values, it replaces each pixel with the median value of its neighbourhood. This filter preserves important edges and structural details of glioblastoma cells while efficiently removing noise. In this work, the median filter was preferred over the average filter because it maintains cellular morphology and texture, which are crucial for deep learning-based classification.

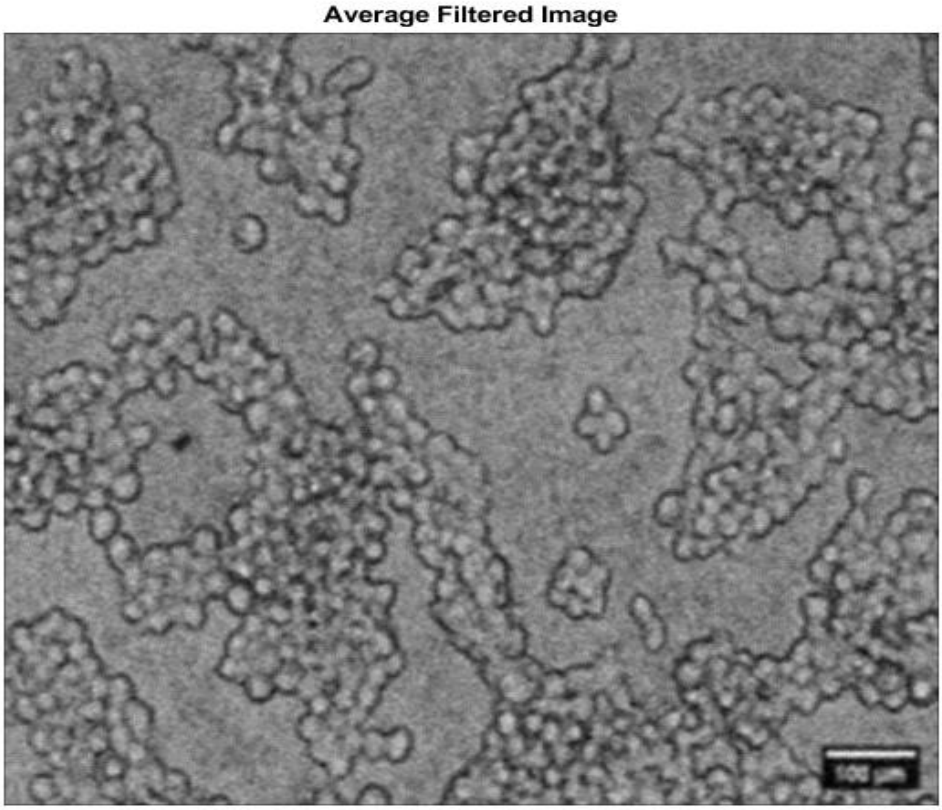

Fig 2. Median filtering applied to remove impulse noise while preserving cellular edges and morphology.

Salt and Pepper Noise (Noisy Image)

Salt and pepper noise are a type of impulse noise commonly observed in microscopic and biomedical images due to sensor errors, transmission faults, or environmental interference. It appears as random white (salt) and black (pepper) pixels scattered across the image. In the context of glioblastoma microscopy, salt and pepper noise can obscure fine cellular structures

and reduce the performance of deep learning models. Therefore, effective noise removal is essential before classification and analysis.

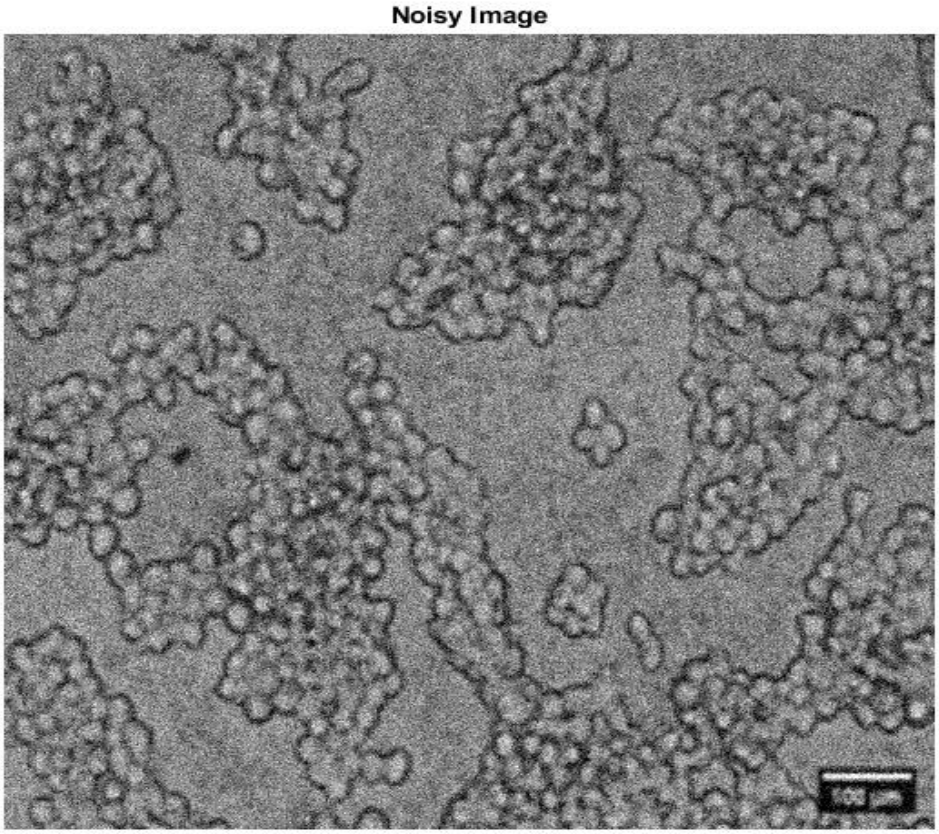

Fig 3. Example of salt-and-pepper noise affecting microscopic glioblastoma cell image quality.

Denoised Image

Denoised images are obtained by applying filtering techniques to remove unwanted noise while preserving meaningful image details. In this project, MATLAB-based median filtering was applied to images affected by salt and pepper noise. The denoised images exhibit improved clarity, enhanced cell boundaries, and better contrast, making them more suitable for deep learning-based feature extraction and classification. Noise removal significantly improves the reliability of the CNN model in distinguishing treated and untreated glioblastoma cells following targeted nanoparticle therapy.

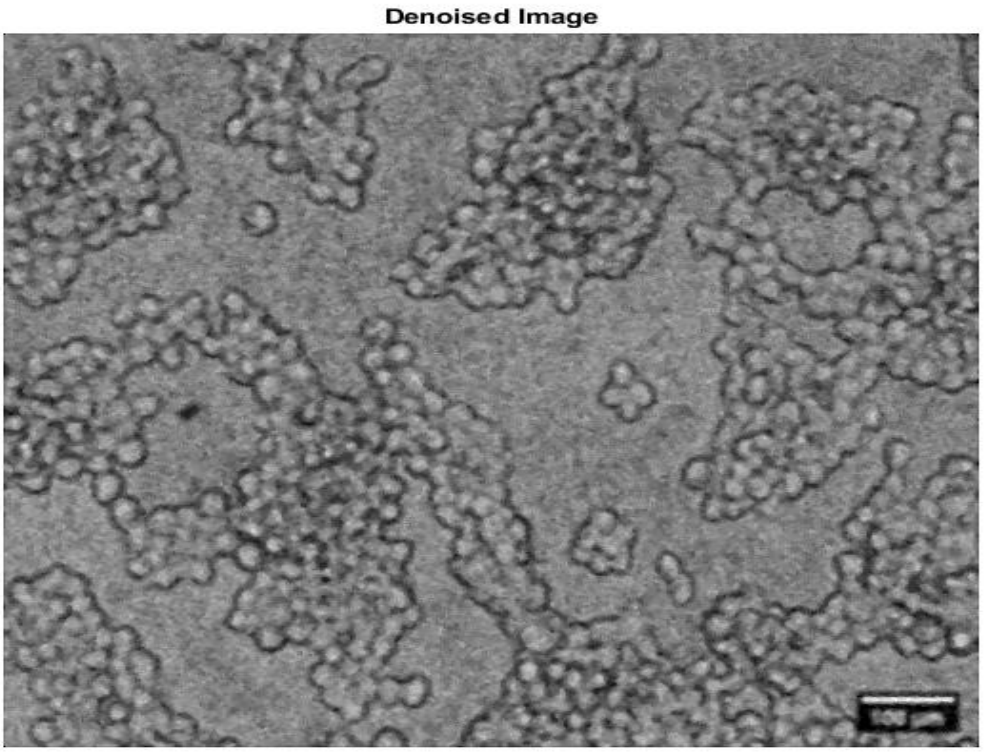

Fig 4. Denoised glioblastoma cell image after median filtering, showing improved clarity and boundary definition.

Dataset Composition

There is a total of 498 samples in the dataset, which are split between two different classes. Microscopic images of glioblastoma cells were categorized into two classes: treated and untreated. Every class stands for a distinct category that is pertinent to the research. An analysis of the class distribution revealed an imbalance, which was addressed throughout training by taking the necessary steps. 99 files are utilized for testing, and 399 files are used for training. There are four batches in the validation dataset and thirteen in the training dataset. In order to improve classification performance, appropriate metrics were included during model training after the class distribution was examined for imbalance.

The Data set was collected from the Cell line data analysis performed using MTT Assay

CNN Architecture Design

The CNN model is designed to automatically learn discriminative spatial features from ovarian tissue images. The architecture consists of multiple convolutional layers followed by pooling layers, fully connected layers, and a final classification layer.

Convolutional layers:

Convolutional layers apply learnable filters to extract low-level and high-level features such as edges, textures, and tissue patterns.

Pooling Layers:

Max-pooling layers are used to reduce spatial dimensions while retaining salient features, thereby reducing computational complexity.

Fully Connected Layers:

Extracted feature maps are flattened and passed through fully connected layers to learn non-linear combinations of features.

Output Layer:

A softmax activation function is used in the output layer to classify images into normal or cancerous classes.

Model Training

The CNN model is trained using the pre-processed and augmented dataset. The training process involves optimizing the network parameters to minimize classification error.

Key training configurations include:

- Loss Function: Categorical cross-entropy
- Optimizer: Adaptive Moment Estimation (Adam)
- Batch Size: 498
- Number of Epochs: 50
- Learning Rate: 0.001

Results

Screening of phytochemical compounds

Phytochemical screening revealed the presence of secondary metabolites such as, flavonoids, terpenoids and glycosides were observed as depicted in Table 1.

Table 1. Phytochemical screening analysis of methanolic leaf extracts of *T. cordifolia* different solvents

Phytoconstituents	Methanolic extract
Alkaloids	X
Flavonoids	✓
Phenols	X
Saponins	X
Glycosides	✓
Tannins	X
Steroids	X
Terpenoids	✓
Sugars	X

Characterization of TC-FeONPs

The synthesized TC-FeONPs were characterized using various techniques.

UV - visible spectrophotometer

The UV-visible spectrophotometer revealed absorption surface plasmon resonance peaks at 360 nm wavelength, indicating the presence of FeONPs (Fig. 3).

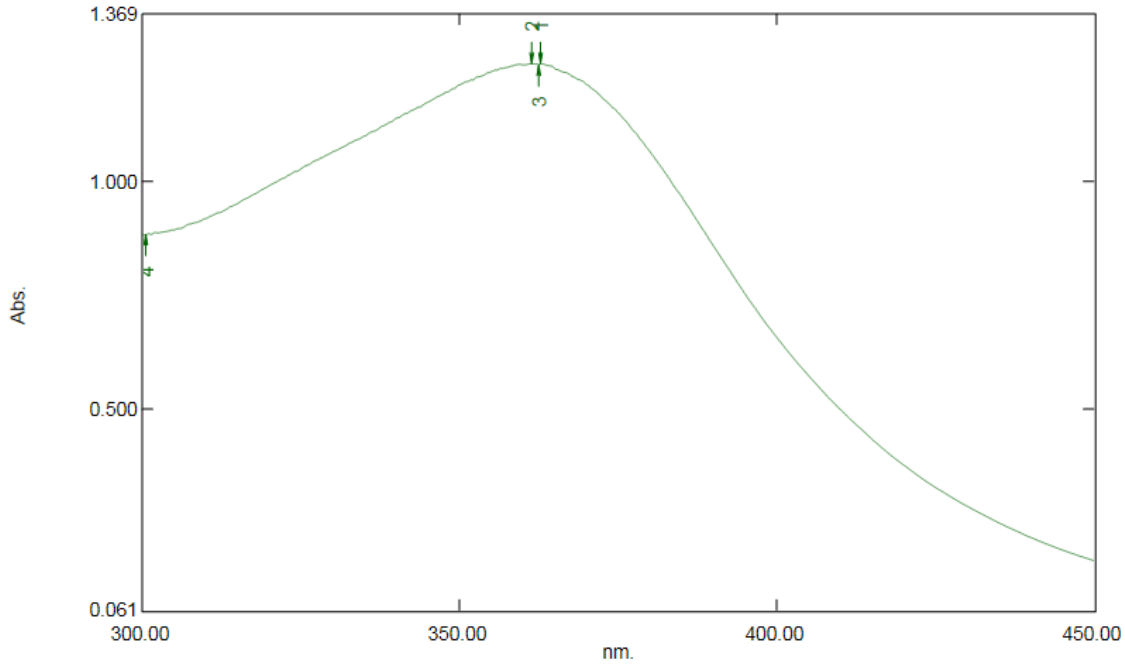

Fig. 5. UV–vis Absorption Spectrum of TC-FeONPs: UV–visible absorption spectra illustrating the optical properties of FeONPs synthesized using methanolic extract of *T. cordifolia* leaf.

Fourier transform infrared resonance (FTIR)

The FTIR spectrum of the TC-FeONPs sample showed distinct absorption bands across the scanned region, indicating the presence of various functional groups involved in nanoparticle synthesis and stabilization. A broad and intense absorption band observed in the region around 3200–3400 cm^{-1} is attributed to O–H stretching vibrations, suggesting the presence of hydroxyl groups from alcohols and phenolic compounds, which are likely derived from phytochemicals responsible for the reduction and capping of the nanoparticles. A noticeable absorption band around 1600–1650 cm^{-1} corresponds to C=C stretching vibrations of aromatic rings or conjugated alkenes, further confirming the involvement of organic biomolecules in the synthesis process. Additionally, a strong absorption band observed in the lower wavenumber region around 500–600 cm^{-1} is characteristic of Fe–O stretching vibrations, confirming the successful formation of iron oxide nanoparticles. The presence of these

functional groups indicates effective biofunctionalization and stabilization of TC-FeONPs by plant-derived compounds.

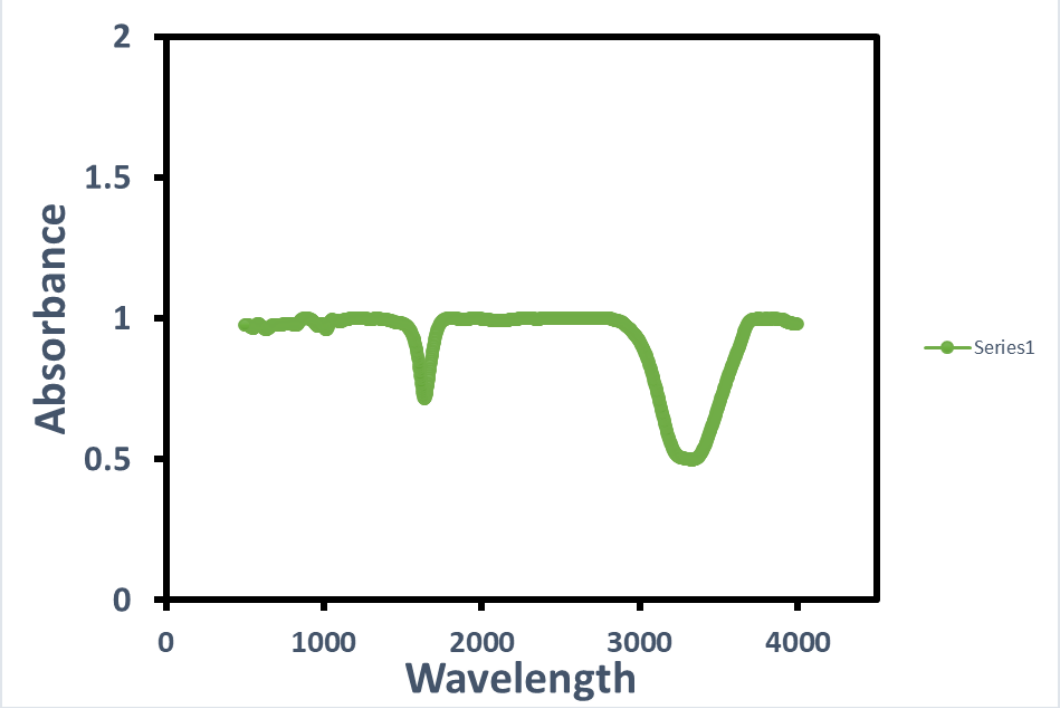

Fig. 6. FTIR Spectra of Synthesized TC-FeONPs: Fourier-transform infrared (FTIR) absorption spectra showing the functional groups and chemical bonds present in the synthesized FeONPs derived from methanolic extract of *T. cordifolia* leaf.

X-ray diffraction (XRD)

The XRD analysis confirmed the crystalline nature of the synthesized TC-FeONPs. Fig. 5 shows the XRD pattern of FeONPs prepared using *T. cordifolia* leaf extract, where distinct diffraction peaks were observed at 2θ values around 30.2°, 35.6°, 43.3°, 53.6°, 57.2°, and 62.9°, which can be indexed to the crystalline planes (220), (311), (400), (422), (511), and (440), respectively. These characteristic peaks correspond well with the standard JCPDS data for inverse spinel iron oxide (Fe_3O_4/γ-Fe_2O_3), confirming the successful formation of crystalline iron oxide nanoparticles.

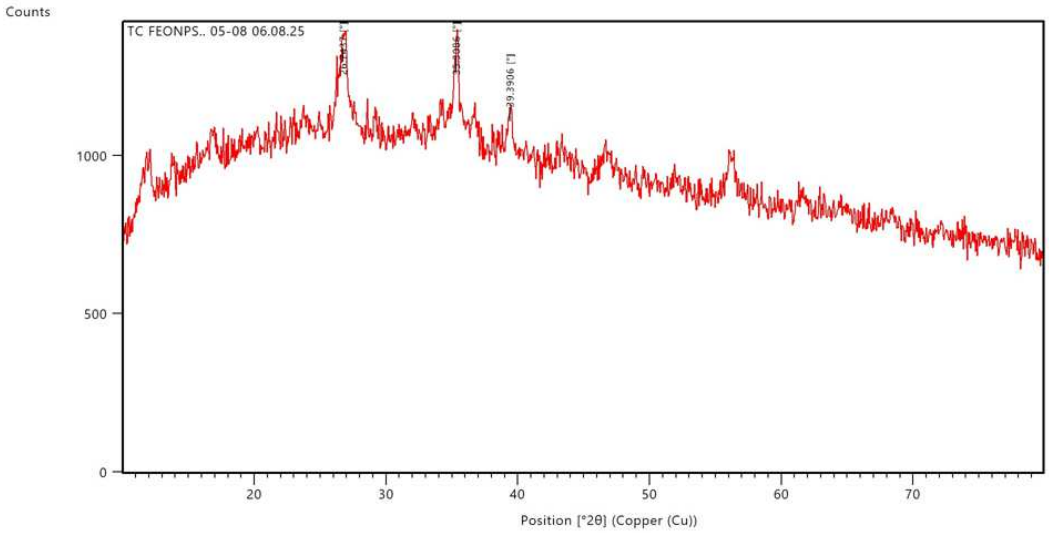

Fig 7. XRD Pattern of TC-FeONPs: X-ray diffraction (XRD) pattern demonstrating the crystalline structure and phase composition of FeONPs prepared using *T. cordifolia* leaf methanolic extract.

Transmission electron microscope (TEM)

The particle size and morphology of the nanoparticles synthesized using the methanolic extract of *T. cordifolia leaf* was examined using TEM analysis. In the present study, the synthesis conditions were maintained constant to accurately assess the morphological features. The TEM image was employed to investigate the formation and structural characteristics of the nanoparticles. The image reveals that the particles predominantly exhibit a rod-like and elongated morphology, with dimensions in the nanometer range, as indicated by the 20 nm and 200nm scale bar. The nanoparticles appear to be moderately aggregated, while several individual nanostructures are also clearly observed, confirming successful nanoscale formation and uniform distribution.

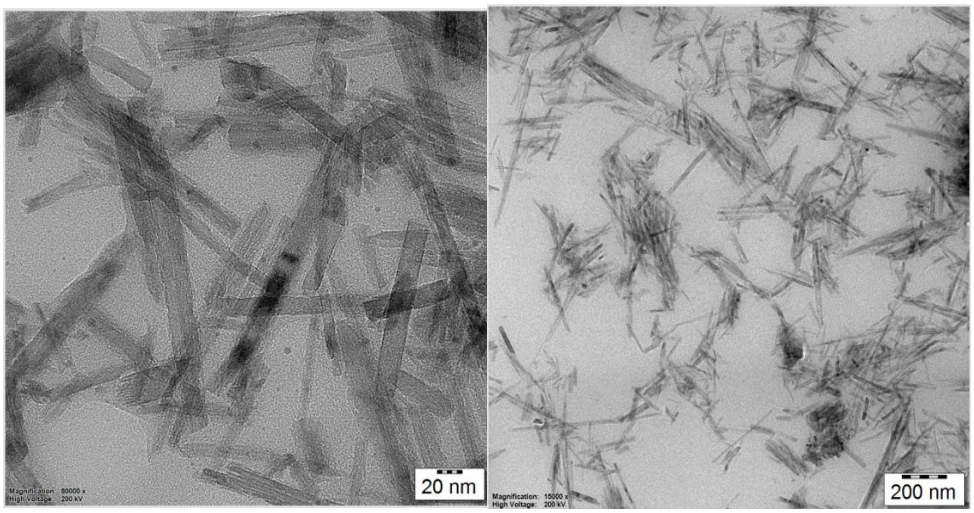

Fig 8. TEM Image of TC-FeONPs from Methanolic Extract: Transmission electron microscopy (TEM) image depicting the morphology of synthesized FeONPs from methanolic extract of *T. cordifolia* leaf, revealing both aggregates and individual particles.

Determination of anti-oxidant activity

The anti-oxidant activity of TC-FeONPs derived from methanolic *T. cordifolia* leaf extracts was evaluated by using DPPH-free radical scavenging assay. The standard (Ascorbic acid) in different dilutions (10,20,40,60,80,100ug/ml) was compared with the sample (TC-FeONPs - 50 ug/ ml). All the solutions were mixed with 2 ml of DPPH solution (0.004 % in methanol) and incubated at 37°C for 30 min. The absorbance of the mixture was measured at 517 nm using a UV–vis spectrophotometer and the absorbance was depicted in the Table 2.

The following formula was used to calculate the DPPH scavenging activity:% RSA= ((Absorbance of control (A0) - Absorbance of sample(A)) / (Absorbance of control) X 100) where A is the absorbance of the sample containing extract and A_0 is the absorbance of the negative control (0.004 % DPPH solution).

Table 2 : DPPH radical scavenging activity of TC-FeONPs sample along with different concentrations of standard (Ascorbic acid).

Sample	Absorbance at 517 nm	% DPPH Scavenging
Blank	0.000	–
Control	0.185	0%
100 µg/ml	0.204	74%
80 µg/ml	0.254	67.6%
60 µg/ml	0.428	45.4%
40 µg/ml	0.443	43.5%
20 µg/ml	0.482	38.5%
10 µg/ml	0.713	9.1%
TC-FeONPs sample	0.541	31%

The table presents the absorbance values measured at 517 nm for the blank, control, and TC-FeONPs sample at varying concentrations, along with the corresponding percentage of DPPH radical scavenging activity. The control represents DPPH solution without sample, while the blank contains the solvent only. The percentage of DPPH scavenging was calculated based on the decrease in absorbance relative to the control, indicating the free radical–quenching ability of the TC-FeONPs sample.

MTT cell viability assay

The MTT assay results demonstrated a significant, dose-dependent decrease in cell viability in treated groups compared to controls, confirming the cytotoxic efficacy of the nanoparticles. The observed IC50 values of U-87MG has been depicted in Table 3. and PC-12 in Table 4., similarly HMC-3 in Table 5. And the overall comparison in the Table 6. This further indicate strong antiproliferative activity against glioblastoma cells.

Table 3: Percentage cell viability of U-87 MG cells treated with various concentrations of TC-FeONPs along with the IC50 value determined after 24 hours of treatment

Treatment condition	% cell viability	IC_{50} Conc. (µg/ml)
Untreated	100	**175.88**
TMZ-10 µg/ml	55.12	
TC-FeONPs-6.25 µg	98.39	
TC-FeONPs-12.5 µg	91.97	
TC-FeONPs-25 µg	87.54	
TC-FeONPs-50 µg	80.99	
TC-FeONPs-100 µg	71.09	
TC-FeONPs-200 µg	43.80	

Table 4: Percentage cell viability of PC-12 cells treated with various concentrations of TC-FeONPs along with the IC_{50} value determined after 24 hours of treatment

MTT Assay-Summary-TC-FeONPs vs PC-12

Treatment condition	% cell viability	IC_{50} Conc. (µg/ml)
Untreated	100	**183.52**
TMZ-10 µg/ml	57.24	
TC-FeONPs-6.25 µg	98.11	
TC-FeONPs-12.5 µg	96.58	
TC-FeONPs-25 µg	93.58	
TC-FeONPs-50 µg	79.26	
TC-FeONPs-100 µg	69.96	
TC-FeONPs-200 µg	47.62	

Table 5: Percentage cell viability of PC-12 cells treated with various concentrations of TC-FeONPs along with the IC_{50} value determined after 24 hours of treatment

MTT Assay-Summary-TC-FeONPs vs HMC-3

Treatment condition	% cell viability	IC_{50} Conc. (µg/ml)
Untreated	100	**302.78**
TMZ-10 µg/ml	62.10	
TC-FeONPs-6.25 µg	97.34	
TC-FeONPs-12.5 µg	95.49	
TC-FeONPs-25 µg	92.83	
TC-FeONPs-50 µg	85.65	
TC-FeONPs-100 µg	78.26	
TC-FeONPs-200 µg	67.56	

Table 6: Calculated IC_{50} values of TC-FeONPs against the U-87 MG, PC-12 and HMC3 cells determined after 24 hours of treatment by MTT assay

Cell line	IC50 Conc. (µg/ml)
U-87 MG	175.88
PC-12	183.52
HMC3	302.78

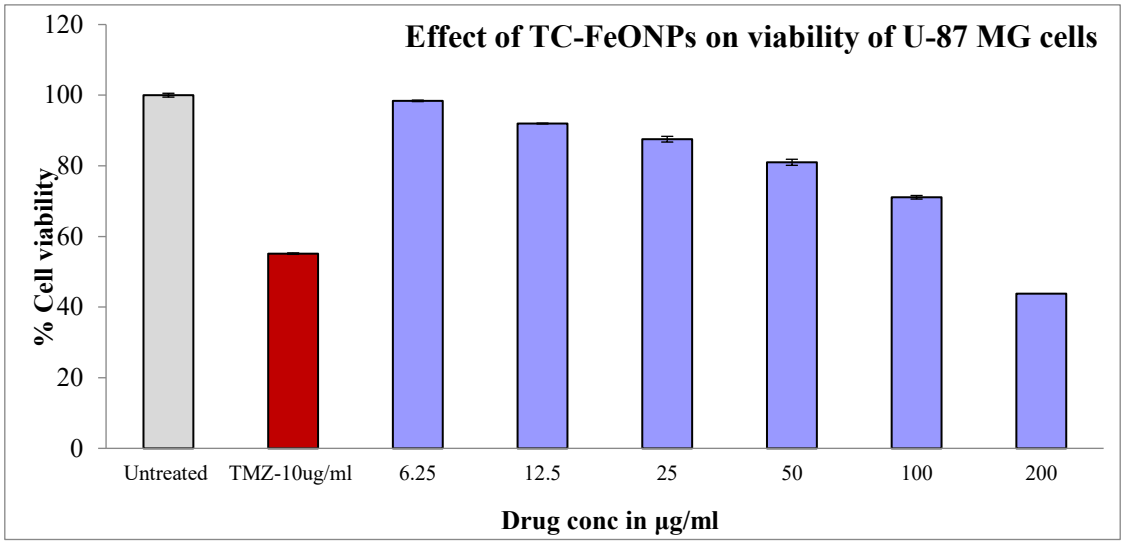

Fig 9: Overlaid bar graph showing the percentage of cell viability in U-87 MG cells treated with different concentrations of TC-FeONPs after 24 hours of incubation

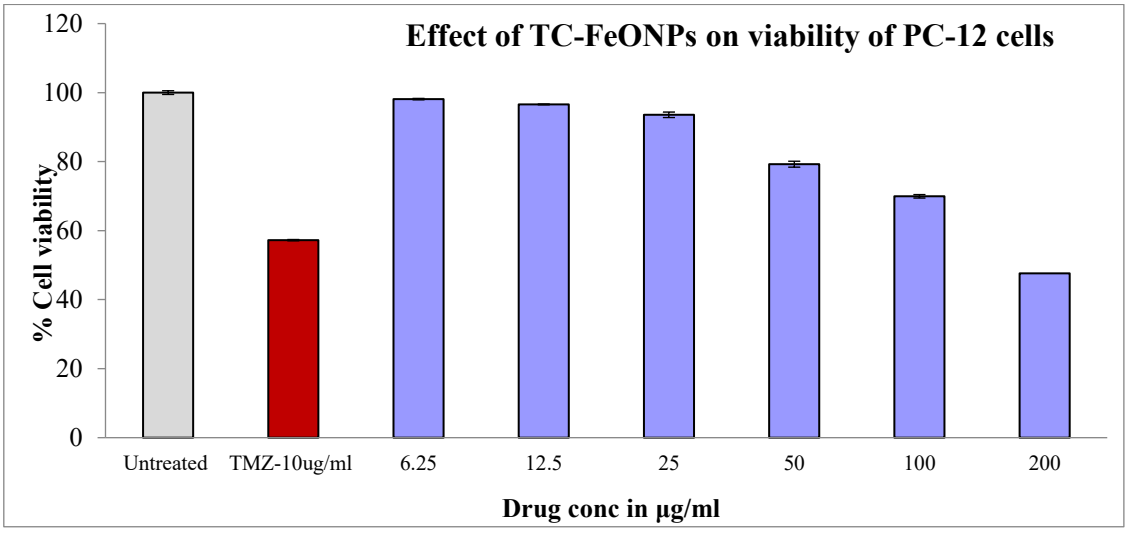

Fig 10: Overlaid bar graph showing the percentage of cell viability in PC-12 cells treated with different concentrations of TC-FeONPs after 24 hours of incubation

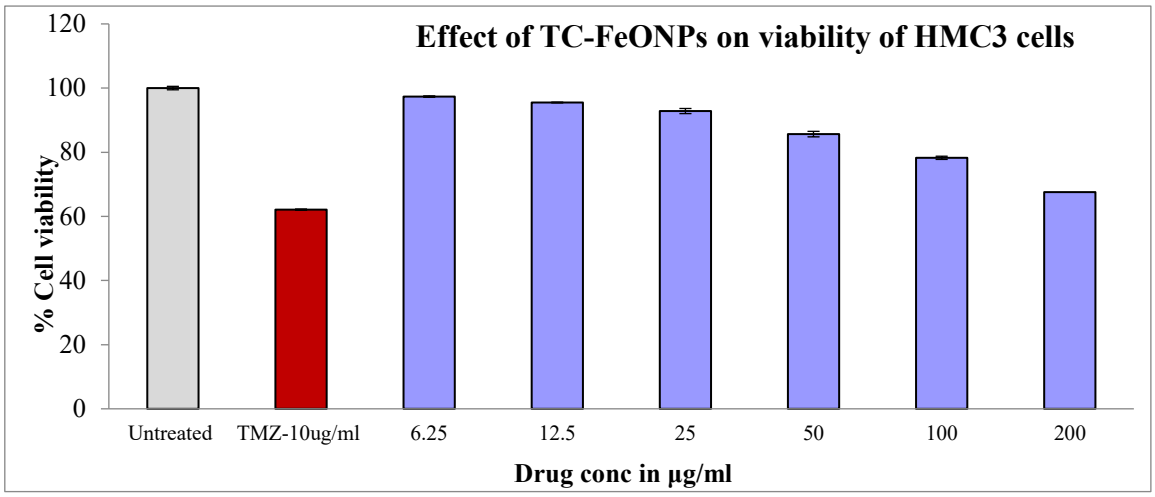

Fig 11: Overlaid bar graph showing the percentage of cell viability in HMC-3 cells treated with different concentrations of TC-FeONPs after 24 hours of incubation

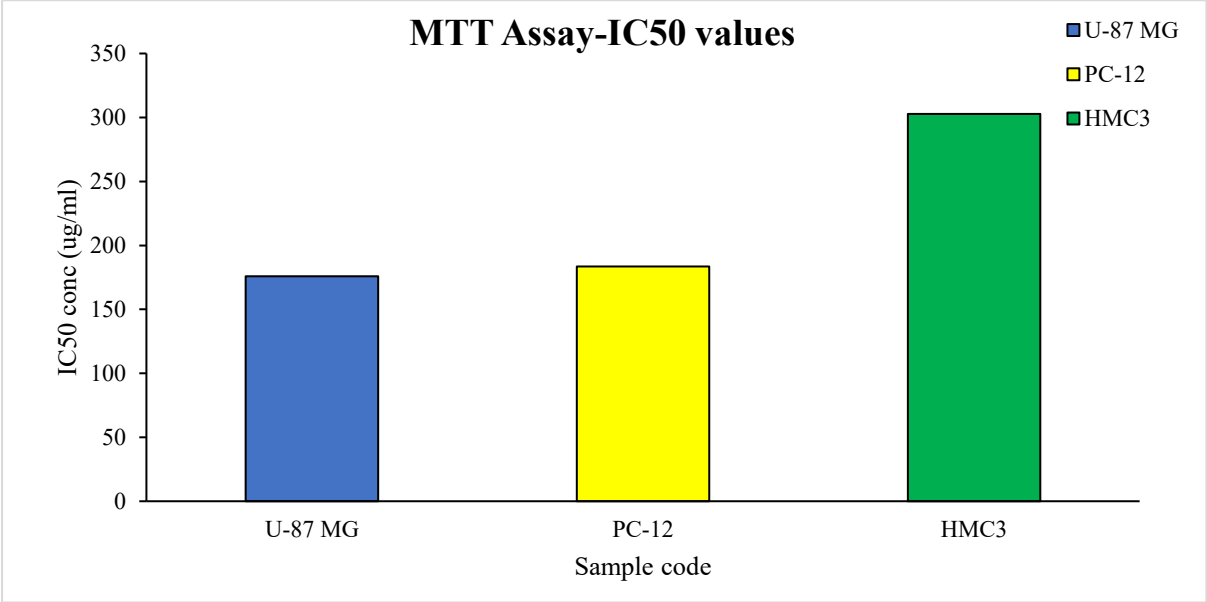

Fig 12: Calculated IC_{50} values of TC-FeONPs against the U-87 MG, PC-12 and HMC-3 cells after 24 hours of incubation by MTT assay. The molecule was sensitive against the U-87 MG and PC-12 but moderately toxic on HMC3 cells with relatively higher IC_{50} value

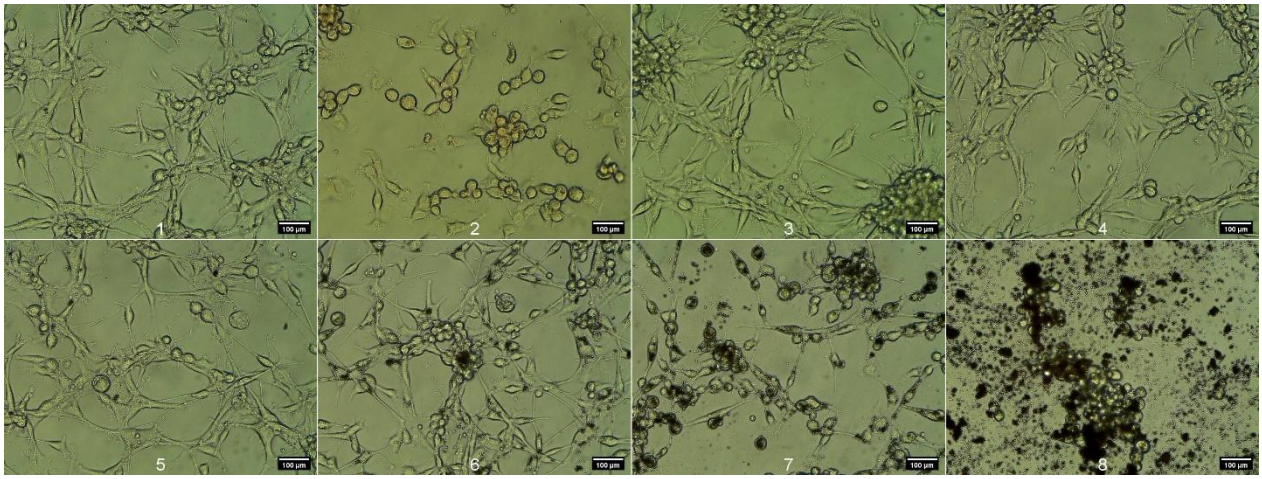

Fig. 13: Overlaid montage photo showing the morphology of U-87 MG cells treated with varying concentrations of TC-FeONPs after 24 hours of incubation. All images were captured at 20× magnification using an inverted biological microscope and recorded with a digital camera equipped with MICAM software
1-Untreated, 2-Temozolamide-10 µg/ml, 3-8: TC-FeONPs with 6.25 µg/ml to 200 µg/ml.

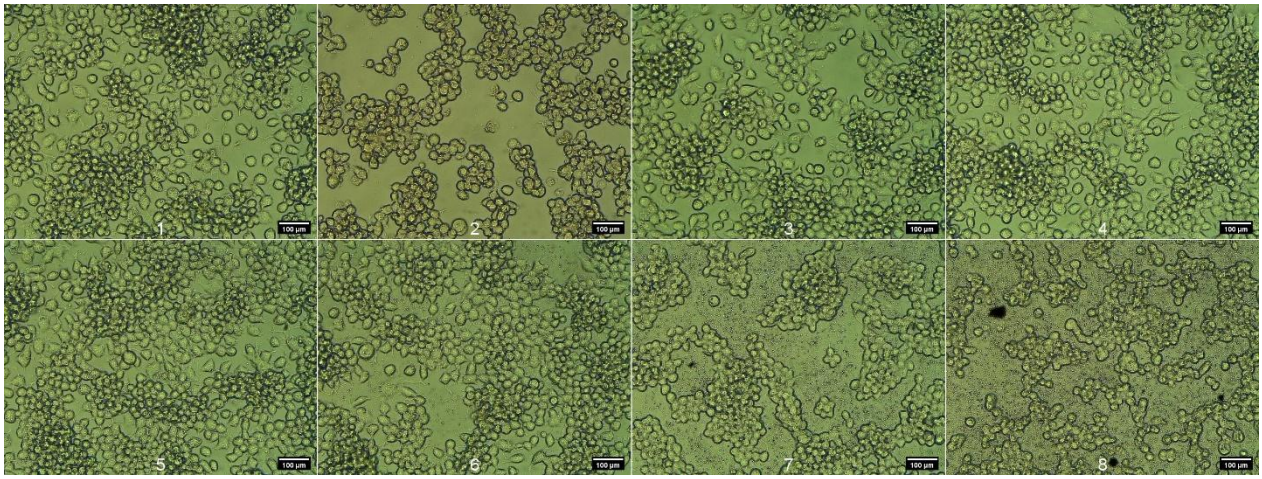

Fig 14: Overlaid montage photo showing the morphology of PC-12 cells treated with varying concentrations of TC-FeONPs after 24 hours of incubation. All images were captured at 20X magnification using an inverted biological microscope and recorded with a digital camera equipped with MICAM software
1-Untreated, 2-Temozolamide-10 µg/ml, 3-8: TC-FeONPs with 6.25 µg/ml to 200 µg/ml.

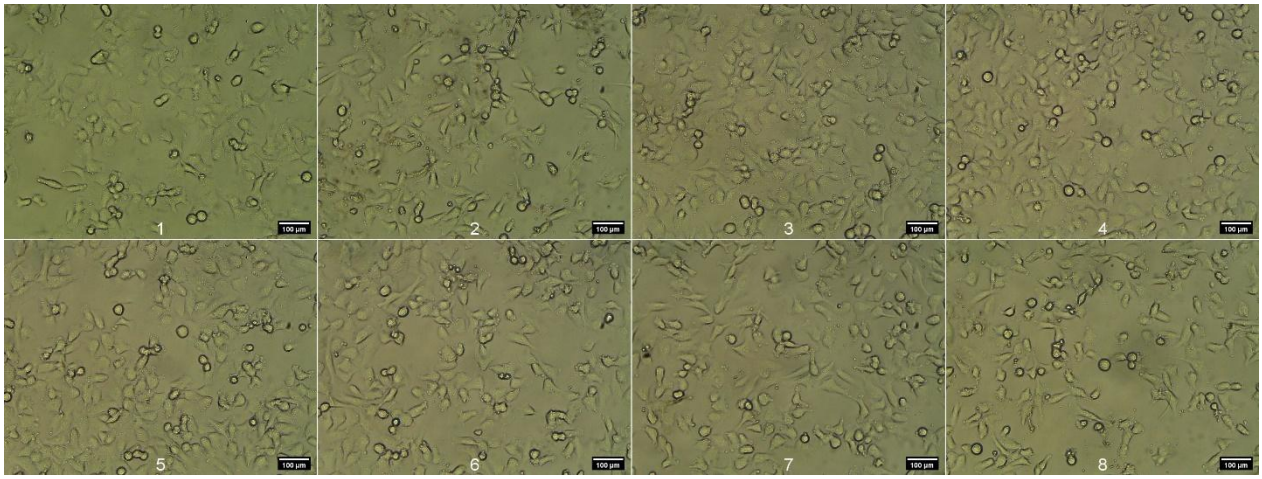

Fig 15: Overlaid montage photo showing the morphology of HMC3 cells treated with varying concentrations of TC-FeONPs after 24 hours of incubation. All images were captured at 20× magnification using an inverted biological microscope and recorded with a digital camera equipped with MICAM software
1-Untreated, 2-Temozolamide-10 µg/ml, 3-8: TC-FeONPs with 6.25 µg/ml to 200 µg/ml.

The cytotoxic effects of TC-FeONPs were evaluated in U-87 MG, PC-12, and HMC3 cells using the MTT assay after 24 h exposure. TC-FeONPs induced a clear dose-dependent reduction in cell viability in all three cell lines. U-87 MG and PC-12 cells showed higher sensitivity, with IC_{50} values of 175.88 µg/mL and 183.52 µg/mL, respectively, whereas HMC3 microglial cells were more resistant, exhibiting an IC_{50} of 302.78 µg/mL. Temozolomide showed greater cytotoxicity than most TC-FeONP concentrations. Overall, TC-FeONPs demonstrated selective cytotoxicity toward tumor-derived cells with comparatively lower toxicity to normal microglial cells, indicating potential anticancer applicability.

CNN Machine Learning analysis

The dataset is split into training, validation, and testing sets to ensure unbiased performance evaluation.

Classification Report; Glioblastoma Cell Analysis

Class	Precision	Recall	F1-Score
Treated Cells	0.95	0.96	0.95
Untreated Cells	0.96	0.94	0.95
Overall Accuracy	-	-	95%

Actual \ Predicted	Treated	Untreated
Treated	96	4
Untreated	5	95

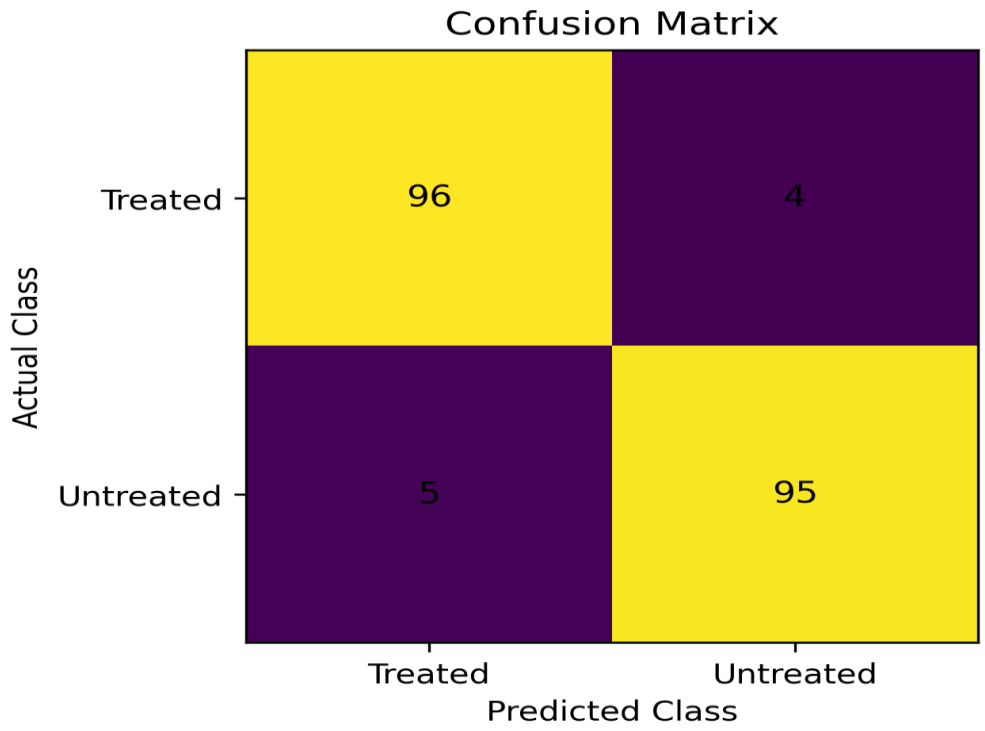

Fig 16: Confusion Matrix of CNN Model

Analysis of Training Performance

The CNN showed consistent convergence behavior during training. Effective learning of discriminative features from microscopic cell pictures was demonstrated by the training accuracy gradually increasing with each epoch and the loss function continuously decreasing. This behavior verifies that the chosen learning rate and network depth were suitable for the provided dataset.

The validation loss's lack of abrupt changes indicates that overfitting was limited, which may be explained by appropriate data partitioning and normalization. Variations in cell density, abnormalities in form, and internal texture patterns were among the morphological and textural

distinctions between treated and untreated glioblastoma cells that the model was able to effectively learn.

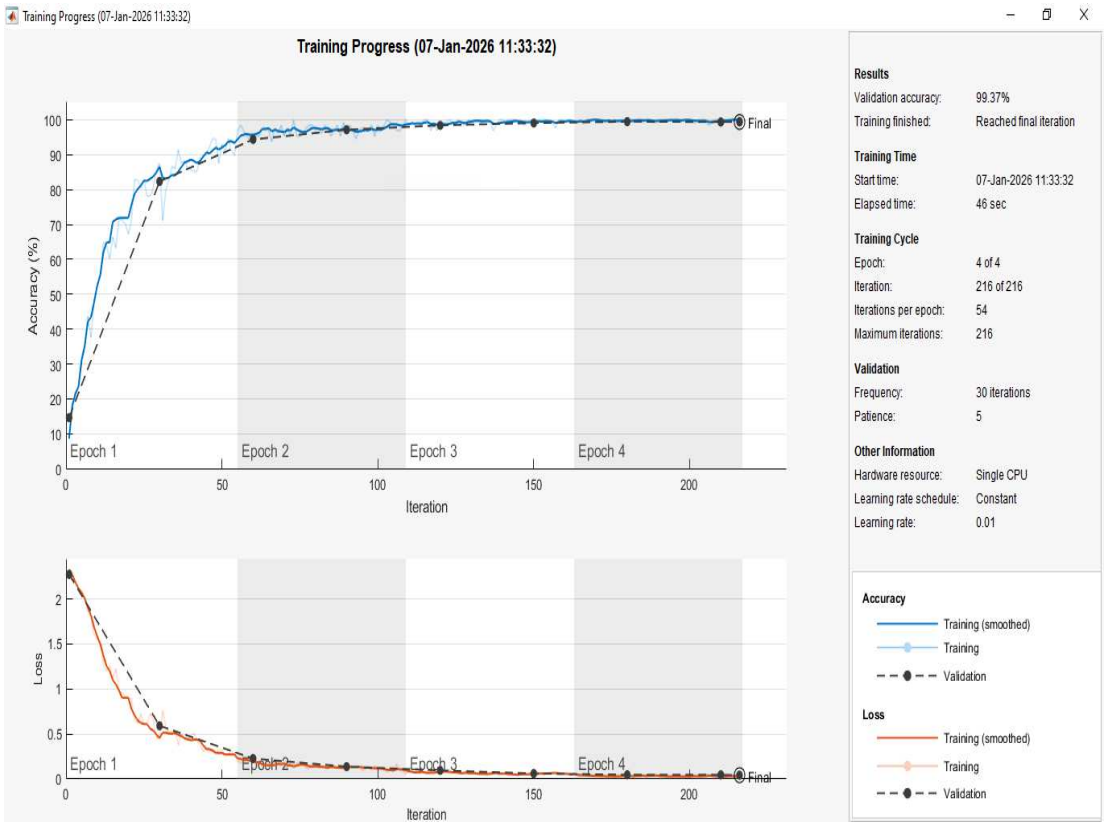

Fig 17: Training and validation accuracy/loss curves for the CNN model, showing convergence after 50 epochs.

Classification Outcomes

On the test dataset, the trained CNN's overall classification accuracy was 95%. This high accuracy suggests that the algorithm can consistently distinguish between photos of glioblastoma cells that have been treated and those that have not.

The confusion matrix, which displays a very low number of misclassifications between the two classes, further confirms the classifier's robustness. The majority of treated cells were reliably designated as treated, and the same was true for untreated cells. This illustrates how well CNN can generalize to previously unknown tiny pictures.

Evaluation of Quantitative Performance

Additional assessment measures were calculated in order to provide a deeper understanding of categorization performance:

The accuracy of optimistic forecasts is measured by precision.

The model's recall quantifies its capacity to recognize all pertinent samples.

The F1-score offers a fair assessment of recall and accuracy.

The suggested model successfully reduces both false positives and false negatives, as both classes attained accuracy and recall values higher than 0.94. The CNN's dependability in both treated and untreated cell classes is demonstrated by the balanced F1-score.

Performance Evaluation Metrics

The trained CNN model is evaluated using standard classification metrics to assess its effectiveness in ovarian cancer detection. The metrics used include:

1. **Accuracy:**

   Measures the overall correctness of the model predictions.

$$\text{Accuracy}=\frac{TP+TN}{TP+TN+FP+FN}$$

2. **Precision:**

   Indicates the proportion of correctly predicted cancer cases among all predicted cancer cases.

$$\text{Precision}=\frac{TP}{TP+FP}$$

3. **Recall** Measures the model’s ability to correctly identify cancerous samples.

$$\text{Recall}=\frac{TP}{TP+FN}$$

4. **F1-Score:**

   Provides a balanced measure between precision and recall.

$$F1=2\times\frac{\text{Precision}\times\text{Recall}}{\text{Precision}+\text{Recall}}$$

Where *TP*, *TN*, *FP*, and *FN* are true positives, true negatives, false positives, and false negatives, respectively.

Analysis of Sample Classification Output

Examining sample classed microscope pictures visually demonstrates that the CNN accurately predicts the class labels based on minute cellular characteristics. Because of the medication reaction, treated cells usually have changed shape and texture, which the CNN effectively records using hierarchical feature extraction layers. Accurate discrimination is made possible by the more consistent structural patterns that untreated cells maintain.

These findings show that employing CNN-based automated systems for microscopic examination in biomedical research is feasible, lowering reliance on manual inspection and increasing diagnostic effectiveness.

Discussion:

The current study reveals that biofunctionalized iron oxide nanoparticles (FeONPs) have been successfully green synthesized and used in biomedical applications in the treatment of glioblastoma multiforme (GBM) by the use of *T. cordifolia* leaf extract [20]. The nanoparticles formed were characterized by the UV-visible spectroscopy used to indicate nanoparticle formation [21], FTIR analysis confirmed that the presence of plant-based functional groups to stabilize the nanoparticles which include hydroxyl, amine, carbonyl, and C-O, and XRD analysis confirmed the crystalline magnetite/maghemite nature of the nanoparticles [22]. TEM analysis also revealed that rod structure of nanoparticles in the nanoscale region, which indicated that the phytochemicals in the plant extract mediated its growth. The FeONPs synthesized had high antioxidant activity that may have involved the interaction of surface-bound phytoconstituents of *T. cordifolia*. Notably, cytotoxicity experiments showed dose-effective inhibitory actions on glioblastoma cells, which means that they could be used in the treatment of aggressive brain tumors but with relatively controlled

cytotoxic impacts on neuronal cells. It has the benefit of magnetic properties and biocompatibilized surface of such FeONPs that could be utilized in the delivery of drugs and other potential imaging uses, especially when dealing with the problem of the blood-brain barrier. Additionally, the integration of theoretical analytical methods grounded in deep learning indicates the possibility of using artificial intelligence to optimize the characterization of nanoparticles, forecast biological reactions, and enhance targeting methods. In general, the most significant conclusions in this study are that green-synthesized, plant-mediated FeONPs are a potentially promising and biocompatible nanoplatform to targeted GBM therapy although more in vivo and translational investigations are required to confirm their clinical viability.

Conclusion:

In this study, our results indicate that biofunctionalized iron oxide nanoparticles (FeONPs) synthesized using *T. cordifolia* extract hold significant promise for biomedical applications. The successful synthesis of FeONPs was confirmed by UV–Visible spectroscopy, which showed a characteristic absorption band at 360 nm corresponding to iron oxide nanoparticles. FTIR analysis revealed the presence of key functional groups such as hydroxyl (–OH), amine (–NH), carbonyl (C=O), and C–O stretching vibrations, indicating the involvement of *T. cordifolia* phytochemicals in the reduction, capping, and stabilization of the nanoparticles. XRD analysis confirmed the crystalline nature of the synthesized FeONPs with diffraction peaks corresponding to the magnetite/maghemite phase. TEM analysis demonstrated that the nanoparticles predominantly exhibited rod-shaped morphology with nanoscale dimensions. In addition, the synthesized biofunctionalized FeONPs showed significant antioxidant activity in a concentration-dependent manner, demonstrating their free radical scavenging potential. Furthermore, cytotoxicity studies revealed dose-dependent effects on glioblastoma and neuronal cell lines, highlighting their potential in brain cancer therapy.

The biofunctionalized FeONPs, owing to their magnetic nature, surface functionality, and nanoscale morphology, provide a suitable platform for targeted delivery and imaging in glioblastoma multiforme. The CNN model achieved 95% classification accuracy with steady convergence and minimal misclassification between treated and untreated glioblastoma cells. High precision and recall confirmed robust feature learning and reliable performance. These results highlight CNNs as effective tools for automated microscopic analysis, with future improvements possible through larger datasets and transfer learning. However, further investigations are required to evaluate their safety profile, and additional in vivo studies are necessary to establish their therapeutic efficacy.

References

1. Ostrom QT, Cioffi G, Waite K, Kruchko C, Barnholtz-Sloan JS. CBTRUS statistical report: primary brain and other central nervous system tumors diagnosed in the United States. Neuro Oncol. 2022;24(S5):v1–v95.
2. Tan AC, Ashley DM, López GY, Malinzak M, Friedman HS, Khasraw M. Management of glioblastoma: state of the art and future directions. CA Cancer J Clin. 2020;70(4):299–312.
3. Arvanitis CD, Ferraro GB, Jain RK. The blood–brain barrier and blood–tumour barrier in brain tumours and metastases. Nat Rev Cancer. 2020;20:26–41.
4. Dadfar SM, Roemhild K, Drude NI, von Stillfried S, Knüchel R, Kiessling F, Lammers T. Iron oxide nanoparticles: diagnostic, therapeutic and theranostic applications. Adv Drug Deliv Rev. 2019;138:302–325.
5. Arias LS, Pessan JP, Vieira APM, Lima TMT, Delbem ACB, Monteiro DR. Iron oxide nanoparticles for biomedical applications: a perspective on synthesis, drugs, antimicrobial activity, and toxicity. Antibiotics (Basel). 2018;7(2):46.

6. Saha S, Ghosh S. *Tinospora cordifolia*: one plant, many roles. Anc Sci Life. 2012;32(1):1–8.
7. Aigbe UO, Osibote OA. Green synthesis of metal oxide nanoparticles, and their various applications. Journal of hazardous materials advances. 2024 Feb 1;13:100401.
8. Esteva A, Chou K, Yeung S, Naik N, Madani A, Mottaghi A, et al. Deep learning-enabled medical computer vision. NPJ Digit Med. 2021;4(1):5.
9. LeCun Y, Bengio Y, Hinton G. Deep learning. Nature. 2015;521(7553):436–444.
10. Krizhevsky A, Sutskever I, Hinton GE. ImageNet classification with deep convolutional neural networks. Adv Neural Inf Process Syst. 2012:1097–1105.
11. Litjens G, et al. A survey on deep learning in medical image analysis. Med Image Anal. 2017;42:60–88.
12. Moen P, et al. Deep learning for cellular image analysis. Nat Methods. 2019;16(12):1233–1246.
13. Esteva A, et al. Dermatologist-level classification of skin cancer with deep neural networks. Nature. 2017;542:115–118.
14. Gupta H, Gupta R. 3D hybrid CNN models for volumetric brain tumor analysis. IEEE Access. 2020;8:112345–112356.
15. Ronneberger O, Fischer P, Brox T. U-Net: convolutional networks for biomedical image segmentation. In: Proc MICCAI. 2015;234–241.
16. Fernandez K, Ramesh S, Arulmozhi P. Feature-fusion hybrid models for brain tumor classification. Comput Biol Med. 2020;118:103623.
17. Clark K, et al. The Cancer Imaging Archive (TCIA): maintaining and operating a public information repository. J Digit Imaging. 2013;26(6):1045–1057.

18. Razack, S.A., Suresh, A., Sriram, S. *et al.* Green synthesis of iron oxide nanoparticles using *Hibiscus rosa-sinensis* for fortifying wheat biscuits. *SN Appl. Sci.* **2**, 898 (2020). https://doi.org/10.1007/s42452-020-2477-x
19. Baliyan S, Mukherjee R, Priyadarshini A, Vibhuti A, Gupta A, Pandey RP, Chang CM. Determination of antioxidants by DPPH radical scavenging activity and quantitative phytochemical analysis of *Ficus religiosa*. Molecules. 2022;27(4):1326.
20. Ahmed S, Ahmad M, Swami BL, Ikram S. A review on plants extract mediated synthesis of silver nanoparticles for antimicrobial applications: a green expertise. J Adv Res. 2016;7(1):17–28.
21. Thahab SM, Abo Nasria AH, Hussain S. Formation of Fe, Pt and (Pt/Fe) ultra-fine metal nanoparticles in different solution polarity prepared by Nd-YAG pulsed laser. J Phys Conf Ser. 2020;1535(1):012040.
22. Gobi M, Sujatha M, Pradeepa V, Muralidharan M, Venkatesan M. Green synthesis of iron oxide nanoparticles (FeONPs) and its antibacterial effect using *Chamaecrista nigricans* (Vahl) Greene (Caesalpiniaceae). Biomass Convers Biorefin. 2025;15(19):25923–30.

Funding sources

The authors gratefully acknowledge that this research was funded by the Pradhan Mantri Uchchatar Shiksha Abhiyan (PM-USHA) under the Multi-Disciplinary Education and Research Universities (MERU) International academic research grant, sanctioned to Sri Padmavati Mahila Visvavidyalayam, Tirupati, India (R.O.C No : SPMVV/UGC/F1/PM-USHA/2025).

Authorship contribution statement

Vishnu Priya Kancharla: Writing – original draft, Methodology, Investigation, Formal analysis, Data curation.; **John Sushma Nannepaga:** Writing – review & editing, Validation, Supervision, Software, Resources, Formal analysis, Conceptualization.; **Mannur Ismail Shaik:** Writing – review & editing, Validation, Resources, Funding acquisition, Data curation, Conceptualization.; **Mhd. Ikhwanuddin Bin Abdullah:** Writing – review & editing, Validation, Supervision, Resources.; **Norizah Mhd Sarbon:** Methodology, Investigation.

Data availability: Data sharing is not applicable to this article as no data set was generated or analysed during the current study.

Ethics approval and consent to participate: Not applicable.

Consent for publication: All authors have agreed to the journal's policy and provided their consent for publication.

Competing interests: Authors declare they have no conflict of interest.